

1 **Unexpected DE3 tide in the southern summer**
2 **mesosphere**

Erich Becker¹, Jens Oberheide²

submitted to Geophys. Res. Lett.

May 5, 2023

Corresponding author: E. Becker, Northwest Research Associates, 3380 Mitchell Ln, Boulder, CO 80301, USA (erich.becker@nwra.com)

¹NorthWest Research Associates, Boulder, CO, USA

²Department of Physics and Astronomy, Clemson University, Clemson, SC, USA

Key Points.

- SABER satellite observations and MERRA-2 reanalysis show a significant DE3 tidal component in the southern summer mesosphere.
- The HIAMCM with resolved gravity waves confirms these observations and shows that the DE3 extends up to ~ 90 km at high latitudes.
- The summer mesospheric DE3 gives a 10-20% contribution to the eastward EPF divergence that drives the equatorward residual circulation.

3 Simulation of the January 2017 period using
 4 a gravity-wave resolving global circulation model
 5 (HIAMCM) reveals a predominant eastward
 6 propagating diurnal tide with zonal wavenum-
 7 ber three (DE3) in the southern summer meso-
 8 sphere from about 60 to 90 km height at mid-
 9 dle to high latitudes. We provide observational
 10 evidence based on MERRA-2 reanalysis and
 11 SABER satellite observations for the validity
 12 of this result. The attenuation of the DE3 be-
 13 neath the mesopause generates a significant
 14 eastward Eliassen-Palm flux divergence that

15 contributes to the residual circulation. We also
16 show that the diurnal tide in the northern sum-
17 mer mesosphere likely consists of mainly east-
18 ward propagating components. These findings
19 contradict the usual assumption of a westward
20 propagating diurnal tide with zonal wavenum-
21 ber one in the summer mesosphere.

1. Introduction

Thermal tides have long been known to represent the strongest wave-related wind and temperature perturbations in the mesosphere and lower thermosphere (MLT) [e.g. *Forbes*, 1984; *Akmaev*, 2001]. The tides relevant in the MLT are generated by the daily cycle of UV absorption by stratospheric ozone, as well as by the absorption of infrared solar insolation by tropospheric water vapor and clouds. This gives rise to so-called migrating tides, that is, tidal components that propagate synchronously with the sun from East to West, such as the diurnal tide with zonal wavenumber $s = 1$ (DW1) and the semi-diurnal tide with $s = 2$ (SW2). Additional tidal forcing is due to the daily cycle of deep moist convection in the intertropical convergence zone. Since this tidal forcing is localized in certain geographical regions, so-called non-migrating tides develop that do not propagate synchronously with the sun [*Hagan and Forbes*, 2002; *Zhang et al.*, 2010a, b]. Non-migrating tides are also formed by the interactions of migrating tides with planetary waves and the mean flow [*Lieberman et al.*, 2014; *Achatz et al.*, 2008]. The most prominent non-migrating component is the diurnal, eastward propagating tide that has $s = 3$, the so-called DE3.

Current understanding of tides is based on linear theory that assumes an isothermal background state at rest and sun-synchronous forcing [*Chapman and Lindzen*, 1969], as well as on linear numerical models that include realistic forcing and background atmospheres [*Hagan and Forbes*, 2002; *Achatz et al.*, 2008; *Oberheide et al.*, 2009]. Such linear models can describe many observations of tides in the MLT, and they agree with the tides

42 simulated by general circulation models (GCMs) [e.g., *Smith*, 2012; *Ward et al.*, 2010; *Liu*
 43 *et al.*, 2010; *Pedatella et al.*, 2016; *Vitharana et al.*, 2019].

44 The morphology of tides can be summarized as follows. The DW1 is the most prominent
 45 component at low and subtropical latitudes up to about 90 km. In the 90-130 km regime
 46 at these latitudes, the DE3 has the largest amplitude in comparison to all other tidal
 47 components. The tides have smaller amplitudes at middle and high latitudes. According
 48 to ground-based measurements, the diurnal tides are most prominent up to about 85-90
 49 km, while semi-diurnal tides account for the strongest tidal variations in the mesopause
 50 region [e.g. *Lübken et al.*, 2011; *Kishore Kumar et al.*, 2014; *Chang et al.*, 2012]. According
 51 to linear models and conventional GCMs, these diurnal and semi-diurnal tides at middle
 52 and high latitudes have predominant contributions from the DW1 below 85-90 km and
 53 from the SW2 around and above the mesopause.

54 In the present study we investigate the question whether the observed diurnal variations
 55 in the extratropical summer mesosphere below ~ 85 -90 km are possibly caused by tidal
 56 components other than the DW1. For this purpose we use a GCM with explicit simulation
 57 of gravity waves (GWs), as well as reanalysis and satellite observations. In Sec. 2 we
 58 describe the model and define our tidal analysis. In Sec. 3 we compare tidal variations
 59 from the model and reanalysis, and we estimate the relevance of the DE3 for the residual
 60 circulation. Section 4 presents a new analysis of SABER temperatures. Our conclusions
 61 are presented in Sec. 5.

2. Model and tidal analysis

We employ the High Altitude Mechanistic general Circulation Model (HIAMCM). This model is based on a standard spectral dynamical core that is extended by non-hydrostatic dynamics and thermodynamics for variable composition. It is run at a T256 spectral horizontal resolution and with 280 atmospheric layers extending up to 4×10^{-9} hPa ($z \sim 400$ -500 km). The HIAMCM includes radiative transfer, water vapor transport, latent heating, full topography, a simple slab ocean model, the full surface energy budget, and simple representations of ion drag in the thermosphere. Macro-turbulent vertical and horizontal diffusion is represented by the Smagorinsky scheme, with both diffusion coefficients depending on the Richardson number. This diffusion scheme accommodates molecular viscosity and molecular heat conduction.

The HIAMCM can be nudged to the three-hourly Modern-Era Retrospective analysis for Research and Applications version 2 (MERRA-2) [Bosilovich *et al.*, 2015]. This nudging is performed in spectral space and is restricted to the large-scale flow such that the resolved GWs are not directly affected by the nudging. More specifically, we interpolate the MERRA-2 wind and temperature fields to the terrain-following grid of the HIAMCM and compute the MERRA-2 spectral representations of relative vorticity, horizontal divergence, and temperature. This allows to nudge the HIAMCM straightforwardly in spectral space. Moreover, all postprocessing routines developed for the HIAMCM can be applied to MERRA-2 as well. Detailed descriptions of the methods and algorithms used in the HIAMCM can be found in *Becker et al.* [2022a], *Becker et al.* [2022a], and *Becker et al.* [2022b].

83 In the following we analyze time series for 1-20 January 2017 and 6-17 July 2006. Before
 84 applying the usual tidal decomposition, we first compute average daily cycles in spectral
 85 space. An average daily cycle from the HIAMCM is defined as follows. We compute
 86 temporal averages of the universal time intervals 23:30-00:30, 01:00-02:00, 02:30-03:30, ...,
 87 and 22:00-23:00, taking all model days of the respective period into account. This leads
 88 to a times series with 16 time stamps centered at universal times 00:00, 01:30, 03:00, ...,
 89 and 22:30. Given that the HIAMCM spectral coefficients are saved every 10 minutes, each
 90 time stamp of the average daily cycle for 1-20 January 2017 represents an average over
 91 $7 \times 20 = 140$ snapshots. This number is $7 \times 12 = 94$ for 6-17 July 2006. In the case of
 92 MERRA-2, snapshots are available every 3 hours. Hence, average daily cycles have 8 time
 93 stamps at universal times of 00:00, 03:00, ..., and 21:00 UT. Each time stamps represents
 94 an average over 20 (12) snapshots for the January 2017 (July 2006) period.

3. Results from the model and reanalysis

3.1. Tidal structure and amplitudes

95 Figure 1 illustrates the total temperature tide at 55°S for 1-20 January 2017 from the
 96 HIAMCM (left column) and MERRA-2 (right column). The first row shows keograms at
 97 0.02 hPa ($z \sim 75$ km), while the second and third rows show longitude-height plots at 00:00
 98 UT and 12:00 UT, respectively. The upper level of MERRA-2 is indicated by horizontal
 99 black lines in panel c-f to facilitate the comparison between the left and right panels.
 100 Figures 1a and b indicate a significant DE3 in the southern summer mesosphere. This DE3
 101 is superposed with other components, particularly a DW1. The DE3 is more prominent
 102 in the HIAMCM, while the DW1 is more prominent in MERRA-2. The longitude-height

plots from the model reveal that the DE3 extends from about 0.1 (60 km) to 0.001 hPa (90 km). The tidal structure in MERRA-2 (panel d,f) agrees with that from the model below 0.015 hPa. In particular, a predominant DW1 from about 5 to 0.3 hPa is seen in both data sets with similar amplitudes and phases. Overall, the total tide is more structured in the HIAMCM than in MERRA-2 because of a higher effective resolution.

Figure 2 shows temperature amplitudes of individual tidal components for 1-20 January 2017. The HIAMCM (MERRA-2) results are shown in the left (right) column. Panels a and b show similar DW1 amplitudes below 0.015 hPa, except for the mesosphere at middle and high latitudes where the DW1 has larger amplitudes in MERRA-2. The DW1 furthermore exhibits maxima in the MLT over the equator and around 30° to 40° latitude in either hemisphere. This behavior is well known from other studies [e.g. *Smith*, 2012, her Fig. 8]. The SW2 from the HIAMCM (panel c) exhibits subtropical maxima in the lower thermosphere, but is also significant at middle to high latitudes in the upper mesosphere. MERRA-2 shows larger SW2 amplitudes in the northern lower mesosphere than the HIAMCM. The SW2 amplitudes in Fig. 2c,d are similar in the stratopause region at low latitudes.

The third row of Fig. 2 shows the amplitudes of the eastward propagating, non-migrating tidal components. Colours show the sum of DE1, DE2, and DE3, while white contours show the DE3. Both the HIAMCM and MERRA-2 indicate a tropical maximum of the DE3 below 0.015 hPa. In the HIAMCM (panel e), this maximum transits into a broad maximum in the lower thermosphere that extends into the subtropics, which is well known from analysis of satellite observations [e.g., *Kumari et al.*, 2020] and GCMs [e.g. *Smith*,

2012, her Fig. 14]. Even though the DE3 gives the main contribution in this regime, the DE1 and DE2 components are also significant. Around 0.0001 hPa, the combined amplitude of the DE components at tropical and subtropical latitudes is significantly larger than the DW1 amplitude.

The main finding of this study is that DE tides exhibit a pronounced maximum in the southern summer upper mesosphere at middle to high latitudes, with the DE3 giving the predominant contribution (Fig. 2e). The HIAMCM and MERRA-2 both show that the DE3 is significant in the mesosphere below 0.015 hPa from about 20°S to 60°S. The HIAMCM indicates that this maximum shifts toward the pole with increasing altitude and has a maximum at 60°S and 0.003 hPa (about 85 km).

This result is quite surprising given the fact that the DE3 is usually found only at and above the mesopause at low latitudes. More specifically, the DE3 is considered to be the superposition of a Kelvin wave-like broad symmetric mode that maximizes above 100 km over the equator and an anti-symmetric tidal mode that maximizes around $\pm 20^\circ$ latitude and 95 km [Oberheide and Forbes, 2008], with both modes exchanging energy in the stratosphere/mesosphere when propagating upward [Zhang et al., 2012]. The 20°S/N amplitude maxima in Fig. 2e in the mesosphere with the transition into a broad amplitude maximum symmetric about the equator at higher altitudes is thus what is expected from tidal theory and observations. However, the presence of the DE3 at 60°S and 0.003 hPa is unexpected and cannot be explained through higher-order Hough modes. This is because the second symmetric and antisymmetric modes both peak equatorward of 30° latitude, and the vertical wavelengths of the third symmetric and antisymmetric modes

are well below 10 km and as such too small for these modes to propagate upward from the troposphere.

Lübken et al. [2011] analyzed lidar temperature measurements performed at the station of Davis (69°S, 78°E, Antarctica) during January 2011. They found a significant diurnal temperature tide in the upper mesosphere with an amplitude of at least 6 K at ~ 85 km (see Fig.2 in their paper). They mentioned that conventional models show much weaker tidal amplitudes in this region. However, a DE3 maximum of about 6 K at 69°S and 0.003 hPa (~ 85 km) as simulated by the HIAMCM (Fig. 2e) is quantitatively consistent with the lidar result. Moreover, when considering Figs. 1c and d, also the phase of this diurnal variation with maximum temperatures around local noon agrees with the lidar result, even though Fig. 1 shows results for 55°S.

The first row in Fig. 3 illustrates the temperature tide at 55°N for 6-17 July 2006 from the HIAMCM and MERRA-2. Comparison to Fig. 1a,b indicates that eastward propagating tidal components are less prominent in the northern than in the southern summer mesosphere. The DW1 appears to be a strong component in MERRA-2, while the picture looks more complicated for the HIAMCM. Figure 3c,d show DW1 and SW2 tidal temperature amplitudes for 6-17 July 2006 from the HIAMCM. These amplitudes are similar to that for January when comparing the respective winter and summer hemispheres. In particular, the DW1 is unexpectedly small in the northern summer mesosphere at middle to high latitude. Figure 3e,f show the DE amplitudes from the HIAMCM and MERRA-2. Strong DE amplitudes are seen in the northern summer mesosphere. However, these components seem to be less important than during January.

169 The HIAMCM shows a maximum north of 60°N between 0.01 and 0.003 hPa of about
 170 3 K due to the sum of DE1, DE2, and DE3, where the DE3 gives a contribution of at
 171 most 1 K (Fig. 3e). This result agrees with lidar observations by *Gerding et al.* [2013]
 172 during June and July from 2010 to 2013 performed at the station of Kühlungsborn (54°N,
 173 11°E). These authors found maximum diurnal variations at ~ 85 km of a few K (see Fig.
 174 4 in their paper), which is much weaker than the aforementioned result for Antarctica.
 175 According to Fig. 3, the DW1 hardly contributes to these diurnal tidal variations.

176 We also note that the DE components account for the main diurnal variations in the
 177 southern winter stratopause region from about 1 to 0.1 hPa at middle to high latitudes
 178 (Figs. 3c-f). This feature was also found by *Sakazaki et al.* [2012] in both satellite observa-
 179 tions and reanalyses. We speculate that these authors did not discover DE components in
 180 the summer mesosphere because their analysis was restricted to altitudes below ~ 65 km.

3.2. Relevance for the general circulation

181 Figures 4a-d show the zonal-mean circulation from the upper stratosphere to the lower
 182 thermosphere from the HIAMCM for 1-20 January 2017 (left column) and 6-17 July 2006
 183 (right column). The HIAMCM simulates reasonably realistic temperatures and zonal
 184 winds (first row). This includes the cold summer mesopause and the transition from
 185 westward to eastward flow above the temperature minimum, the subtropical mesospheric
 186 jet in the winter hemisphere, as well as eastward winds at high latitudes in the win-
 187 ter MLT. There are important hemispheric differences when comparing July to January.
 188 These include a stronger eastward flow and stronger westward Eliassen-Palm flux (EPF)
 189 divergence in the winter mesosphere, stronger absolute EPF divergence in the upper meso-

sphere and a stronger summer-to-winter pole residual circulation, and a colder summer polar mesopause. These hemispheric differences are consistent with the interhemispheric coupling mechanism [Karlsson and Becker, 2016, e.g.]. There is stronger eastward EPF divergence in the winter mesopause region during July because of stronger secondary GWs in the southern winter MLT [e.g., Becker and Vadas, 2018; Vadas and Becker, 2019; Harvey *et al.*, 2022]. Also the westward EPF divergence in the summer lower thermosphere is stronger during July. As a result of these hemispheric differences, the reversed residual circulation cell in the lower thermosphere [Smith *et al.*, 2011] is stronger during July than January and extends from pole to pole.

Figures 4e,f show the EPF divergence in the summer MLT that are due to the resolved GWs (colors). We compute the GW EPF divergence by subtracting the EPF divergence that is due to planetary-scale waves from the complete EPF divergence. The latter is defined by retaining only total horizontal wavenumbers up to 30 and zonal wavenumbers from 1 to 6. The so-defined GW EPF divergence exceeds $120 \text{ m s}^{-1} \text{ d}^{-1}$ at 50°N to 60°N around 0.001 hPa during July, which is comparable to estimates from GW schemes [e.g. Fomichev *et al.*, 2002, their Fig. 10]. In the HIAMCM, however, this GW drag is too high in altitude by $\sim 5 \text{ km}$. As a result, also the summer mesopause and the zonal wind reversal are too high in altitude by $\sim 5 \text{ km}$. Superposed in Figs. 4e,f is the tidal EPF divergence that is computed from the average daily cycle (contours). The HIAMCM shows an eastward tidal EPF divergence that maximizes around 0.003 hPa (85 km) and exceeds $15 \text{ m s}^{-1} \text{ d}^{-1}$ in the southern summer mesosphere. Hence, the attenuation of the DE3 beneath the summer mesopause gives rise to a significant contribution (10-20%) to

the driving of the equatorward residual circulation. The corresponding effect during July is very small.

4. Tidal components in the summer mesosphere from SABER

MLT temperatures are routinely measured by the Sounding the Atmosphere using Broadband Emission Radiometry (SABER) instrument onboard the TIMED satellite [Russell III et al., 1999]. Standard tidal diagnostics of SABER has been detailed in earlier papers [i.e., Forbes et al., 2008] and requires to combine 60 days of observations for local solar time coverage. Furthermore, the spacecraft yaws every 60 days, which changes the latitude coverage of the measurements from 55°S-85°N to 85°S-55°N, and vice versa. Yaws happened on 31 December 2016 and on 14 July 2006, and SABER was looking into the wrong hemisphere in January 2017 and late July 2006. We therefore compare here observations for 21-30 December 2016 to the model results for January 2017, and we compare roughly the same time periods for July 2006. To avoid the 60-day averaging, we obtain a DE3 amplitude proxy as follows. For the 10-day periods preceding the yaws, we fit zonal wave number 4 separately to observations made on the ascending (asc) and descending (dsc) orbit nodes. A wave 4 observed in the satellite local solar time frame of reference is, generally speaking, a superposition of a stationary wave 4 and various non-migrating tides (DW5, DE3, SW6, SE2, TW7, and TE1) [Oberheide et al., 2011]. The local time difference between the asc and dsc observations in the hemisphere of interest is about 14 hours. Differencing asc and dsc fits thus amplifies the DE3 amplitudes (factor of 2) while minimizing semidiurnal, terdiurnal, and stationary wave signals.

Figure 5 shows the results for December 2016 and July 2006. The patterns are structurally similar to the HIAMCM and MERRA-2 results (Figs. 2e,f and 3e,f). This includes a stronger DE3 in the low-latitude MLT during July. In particular, SABER shows a pronounced middle to high-latitude DE3 maximum in the summer mesosphere during December that tilts towards higher latitudes with altitude. A maximal DE3 amplitude of ~ 3 K is found at ~ 75 km and 50° S. The middle to high-latitude DE3 in July from SABER is less pronounced, which is also consistent with the model result. Note that the high-latitude SABER maximum for December does not extend much above 80 km. Whether this difference to the HIAMCM is due to some interference in the asc-dsc differences or other effects cannot be resolved with the data at hand.

5. Conclusions

We reported about an unexpected DE3 tide in the southern summer mesosphere at middle to high latitudes. We first found this DE3 in a simulation of January 2017 using a GW-resolving GCM (HIAMCM). We proved that the model result is consistent with MERRA-2 reanalysis and a new tidal analysis of SABER temperature data. Moreover, the large diurnal tidal amplitude from the DE3 is quantitatively consistent with previous lidar measurements at Antarctica [Lübken *et al.*, 2011]. From the zonal-mean analysis we concluded that the attenuation of the DE3 beneath the summer mesopause gives a significant eastward EPF divergence that contributes about 10-20% to the driving of the residual circulation. We also analyzed a period during July 2006 and found that the diurnal tide in the northern summer mesosphere is mainly a combination of eastward non-migrating tides (DE1, DE2, and DE3). The overall diurnal tide is weaker than in the

southern summer mesosphere, which is in agreement with ground-based measurements by *Gerding et al.* [2013].

A strong DE3 in the southern summer mesosphere is usually not found in linear models or global circulation models with conventional parameterization of GWs. Such models exclude important aspects of GW feedback on the tides [e.g. *Senf and Achatz*, 2011]. This suggests that the unexpected DE3 in the southern summer mesosphere is simulated only in models that account for the fully nonlinear and time-dependent GW-tidal interactions.

We analyzed only the northern winter 2016-2017 to document the DE3 in the southern summer mesosphere. Analysis of other periods are necessary to determine whether our results apply in a more general sense. Also, a detailed investigation of the GW-tidal interactions and other possible mechanisms that may explain the DE3 in the southern summer mesosphere and hemispheric differences of tidal components is demanded by our findings. These efforts are, however, beyond the scope of this paper and will be subject to future studies.

Acknowledgments. EB acknowledges support by NASA grant 80NSSC19K0834. JO was supported by NASA grants 80NSSC19K0258 and 80NSSC20K1353. We thank the Leibniz Institute of Atmospheric Physics at the University of Rostock and the NASA High-End Computing Capability (HECC) for providing HPC facilities used in this study.

Open Research. Model documentations can be found in in *Becker and Vadas* [2020], *Becker et al.* [2022a], and *Becker et al.* [2022b]. Model data shown in this study can be downloaded from NWRA’s website under <https://www.cora.nwra.com/~erich.becker/Becker-Oberheide-GRL-2023-files>.

The MERRA-2 reanalysis data are publicly available at

<https://goldsmr5.gesdisc.eosdis.nasa.gov/data/MERRA2/M2I3NVASM.5.12.4/2017>.

SABER v2.07 data can be downloaded from

<https://saber.gats-inc.com/data.php>.

References

Achatz, U., N. Grieger, and H. Schmidt (2008), Mechanisms controlling the diurnal solar tide: Analysis using a gcm and a linear model, *J. Geophys. Res.*, *113*(A08303), doi:10.1029/2007JA012967.

Akmaev, R. A. (2001), Simulation of large-scale dynamics in the mesosphere and lower thermosphere with the doppler-spread parameterization of gravity waves 2. eddy mixing and the diurnal tide, *J. Geophys. Res.*, *106*(D1), 1205–1213, doi:10.1029/2000JD900520.

Becker, E., and S. L. Vadas (2018), Secondary gravity waves in the winter mesosphere: Results from a high-resolution global circulation model, *J. Geophys. Res. Atmos.*, *123*, doi:10.1002/2017JD027460.

Becker, E., and S. L. Vadas (2020), Explicit global simulation of gravity waves in the thermosphere, *J. Geophys. Res. Space Phys.*, doi:10.1029/2020JA028034.

Becker, E., S. L. Vadas, K. Bossert, V. L. Harvey, C. Zülicke, and L. Hoffmann (2022a), A high-resolution whole-atmosphere model with resolved gravity waves and specified large-scale dynamics in the troposphere and stratosphere, *J. Geophys. Res. Atmos.*, *127*(e2021JD035018), doi:10.1029/2021JD035018.

Becker, E., L. Goncharenko, V. L. Harvey, and S. L. Vadas (2022b), Multi-step vertical coupling during the january 2017 sudden stratospheric warming, *J. Geophys. Res. Space*

296 *Phys.*, 127(e2022JA030866), doi:10.1029/2022JA030866.
 297 Bosilovich, M. G., S. Akella, L. Coy, R. Cullather, C. Draper, R. Gelaro, R. Kovach,
 298 Q. Liu, A. Molod, P. Norris, K. Wargan, W. Chao, R. Reichle, L. Takacs, Y. Vikhliayev,
 299 S. Bloom, A. Collin, S. Firth, G. Labow, G. Partyka, S. Pawson, O. Reale, S. D. Schu-
 300 bert, , and M. Suarez (2015), MERRA-2: Initial evaluation of the climate, *NASA Tech.*
 301 *Rep. Series on Global Modeling and Data Assimilation* , *NASA/TM-2015-104606/Vol.*
 302 *43*, Goddard Space Flight Center.
 303 Chang, L. C., W. E. Ward, S. E. Palo, J. Du, D.-Y. Wang, H.-L. Liu, M. E. Hagan,
 304 Y. Portnyagin, J. Oberheide, L. P. Goncharenko, T. Nakamura, P. Hoffmann, W. Singer,
 305 P. Batista, B. Clemesha, A. H. Manson, D. M. Riggan, C.-Y. She, T. Tsuda, and T. Yuan
 306 (2012), Comparison of diurnal tide in models and ground-based observations during the
 307 2005 equinox CAWSES tidal campaign, *J. Atmos. Sol. Terr. Phys.*, 78-79, 19–30, doi:
 308 10.1016/j.jastp.2010.12.0104.
 309 Chapman, S., and R. S. Lindzen (1969), Atmospheric tides, *Space Sci. Rev.*, 10(1), 3–188,
 310 doi:10.1007/BF00171584.
 311 Fomichev, V. I., W. E. Ward, S. R. Beagley, C. McLandress, J. C. McConnell, N. A.
 312 McFarlane, and T. G. Shepherd (2002), Extended Canadian Middle Atmosphere Model:
 313 Zonal-mean climatology and physical parameterizations, *J. Geophys. Res.*, 107(D10),
 314 ACL9–1–ACL9–14, doi:10.1029/2001JD000479.
 315 Forbes, J. M. (1984), Middle atmosphere tides, *J. Atmos. Terr. Phys.*, 46(11), 1049–1067,
 316 doi:10.1016/0021-9169(84)90008-4.

- Forbes, J. M., X. Zhang, S. Palo, J. Russell, C. J. Mertens, , and M. Mlynczak (2008),
Tidal variability in the ionospheric dynamo region, *J. Geophys. Res. Space Phys.*,
113(A02310), doi:10.1029/2007JA012737.
- Gerding, M., M. Kopp, P. Hoffmann, J. Höffner, and F.-J. Lübken (2013), Diur-
nal variations of midlatitude NLC parameters observed by daylight-capable lidar
and their relation to ambient parameters, *Geophys. Res. Lett.*, *40*, 6390–6394, doi:
10.1002/2013GL057955.
- Hagan, M. E., and J. M. Forbes (2002), Migrating and nonmigrating diurnal tides in the
middle and upper atmosphere excited by tropospheric latent heat release, *J. Geophys.*
Res., *107*(D24), doi:10.1029/2001JD001236.
- Harvey, V. L., N. Pedatella, E. Becker, and C. E. Randall (2022), Evaluation of po-
lar winter mesopause wind in WACCMX+DART, *J. Geophys. Res. Atmos.*, doi:
10.1029/2022JD037063.
- Karlsson, B., and E. Becker (2016), How does interhemispheric coupling contribute to
cool down the summer polar mesosphere?, *J. Clim.*, *29*, 8807–8821, doi:10.1175/JCLI-
D-16-0231.1.
- Kishore Kumar, G., W. Singer, J. Oberheide, N. Grieger, P. P. Batista, D. M.
Riggin, H. Schmidt, and B. R. Clemesha (2014), Diurnal tides at low latitudes:
Radar, satellite, and model results, *J. Atmos. Sol. Terr. Phys.*, *118*, 96–105, doi:
10.1016/j.jastp.2013.07.005.
- Kumari, K., J. Oberheide, and X. Lu (2020), The tidal response in the meosphere/lower
thermosphere to the Madden-Julian oscillation observed by SABER, *Geophys. Res.*

Lett., 47(e2020GL089172), doi:10.1029/2020GL089172.

Lieberman, R. S., J. Oberheide, M. E. Hagan, E. E. Remsberg, and L. L. Gordley (2014), Variability of diurnal tides and planetary waves during november 1978–may 1979, *J. . Atmos. Sol. Terr. Phys.*, 66, 571–528, doi:10.1016/j.jastp.2004.01.006.

Liu, H.-L., B. T. Foster, M. E. Hagan, J. M. McInerney, A. Maute, L. Qian, A. D. Richmond, R. G. Roble, S. C. Solomon, R. R. Garcia, D. Kinnison, D. R. Marsh, A. K. Smith, J. Richter, F. Sassi, and J. Oberheide (2010), Thermosphere extension of the whole atmosphere community climate model, *J. Geophys. Res.*, 115(A12301), doi:10.1029/2010JA015586.

Lübken, F.-J., J. Höffner, T. P. Viehl, B. Kaifler, and R. J. Morris (2011), First measurements of thermal tides in the summer mesopause region at Antarctic latitudes, *Geophys. Res. Lett.*, 38, doi:10.1029/2011GL050045.

Oberheide, J., and J. M. Forbes (2008), Tidal propagation of deep tropical cloud signatures into the thermosphere from TIMED observations, *Geophys. Res. Lett.*, 35(L04816114), doi:10.1029/2007GL032397.

Oberheide, J., J. M. Forbes, K. Häusler, Q. Wu, and S. L. Bruinsma (2009), Tropospheric tides from 80 to 400 km: Propagation, interannual variability, and solar cycle effects, *J. Geophys. Res.*, 114(D00I05), doi:10.1029/2009JD012388.

Oberheide, J., J. M. Forbes, X. Zhang, and S. L. Bruinsma (2011), Wave-driven variability in the ionosphere-thermosphere-mesosphere system from timed observations: What contributes to the “wave 4”?, *J. Geophys. Res.*, 116(A01306), doi:10.1029/2010JA015911.

- Pedatella, N. M., J. Oberheide, E. K. S. a nd H.-L. Liu, J. L. Anderson, and K. Reader
(2016), Short-term nonmigrating tide variability in the mesosphere, thermosphere, and
ionosphere, *J. Geophys. Res. Space Phys.*, *121*, 3621–3633, doi:10.1002/2016JA022528.
- Russell III, J. M., M. G. Mlynczak, L. L. Gordley, J. J. Tansock Jr., and R. W. Esplin
(1999), Overview of the saber experiment and preliminary calibration results, *Proc.
spie 3756*, Optical Spectroscopic Techniques and Instrumentation for Atmospheric and
Space Research III (20 October 1999), doi:10.1117/12.366382.
- Sakazaki, T., M. Fujiwara, X. Zhang, M. E. Hagan, and J. M. Forbes (2012), Diurnal
tides from the troposphere to the lower mesosphere as deduced from TIMED/SABER
satellite data and six global reanalysis data sets, *J. Geophys. Res.*, *117*(D13108), doi:
10.1029/2011JD017117.
- Senf, F., and U. Achatz (2011), On the impact of middle-atmosphere thermal tides
on the propagation and dissipation of gravity waves, *J. Geophys. Res.*, *116*, doi:
10.1029/2011JD015794.
- Smith, A. K. (2012), Global dynamics of the MLT, *Surv. Geophys.*, *33*, 1177–1230, doi:
10.1007/s10712-012-9196-9.
- Smith, A. K., R. R. Garcia, D. R. Marsh, and J. H. Richter (2011), WACCM simulations of
the mean circulation and trace species transport in the winter mesosphere, *J. Geophys.
Res.*, *116*(D20115), doi:10.1029/2011JD016083.
- Vadas, S. L., and E. Becker (2019), Numerical modeling of the generation of tertiary
gravity waves in the mesosphere and thermosphere during strong mountain wave events
over the Southern Andes, *J. Geophys. Res. Space Phys.*, doi:10.1029/2019JA026694.

- 382 Vitharana, A., X. Zhu, J. Du, J. Oberheide, and W. Ward (2019), Statistical modeling
383 of tidal weather in the mesosphere and lower thermosphere, *J. Geophys. Res. Atmos.*,
384 *124*, 9011–9027, doi:10.1029/2019JD030573.
- 385 Ward, W. E., J. Oberheide, L. P. Goncharenko, T. Nakamura, P. Hoffmann, W. Singer,
386 L. C. Chang, J. Du, D.-Y. Wang, P. Batista, B. Clemesha, A. H. Manson, C. Meek, D. M.
387 Riggan, C.-Y. She, T. Tsuda, and T. Yuan (2010), On the consistency of model, ground-
388 based and satellite observations of tidal signatures: Initial results from the cawses tidal
389 campaigns, *J. Geophys. Res.*, *115*(D07107), doi:10.1029/2009JD012593.
- 390 Zhang, X., J. M. Forbes, and M. E. Hagan (2010a), Longitudinal variation of tides in
391 the mlt region: 1. Tides driven by troposphere net radiative heating, *J. Geophys. Res.*,
392 *115*(A06316), doi:10.1029/2009JA014897.
- 393 Zhang, X., J. M. Forbes, and M. E. Hagan (2010b), Longitudinal variation of tides in the
394 mlt region: 2. Relative effects of solar radiative and latent heating, *J. Geophys. Res.*,
395 *115*(A06317), doi:10.1029/2009JA014898.
- 396 Zhang, X., J. M. Forbes, and M. E. Hagan (2012), Seasonal-latitudinal variation of the
397 eastward-propagating diurnal tide with zonal wavenumber 3 in the MLT: Influences of
398 heating and background wind distribution, *J. Atnos. Sol.-Terr. Phys.*, *78-79*, 37–43,
399 doi:10.1016/j.jastp.2011.03.005.

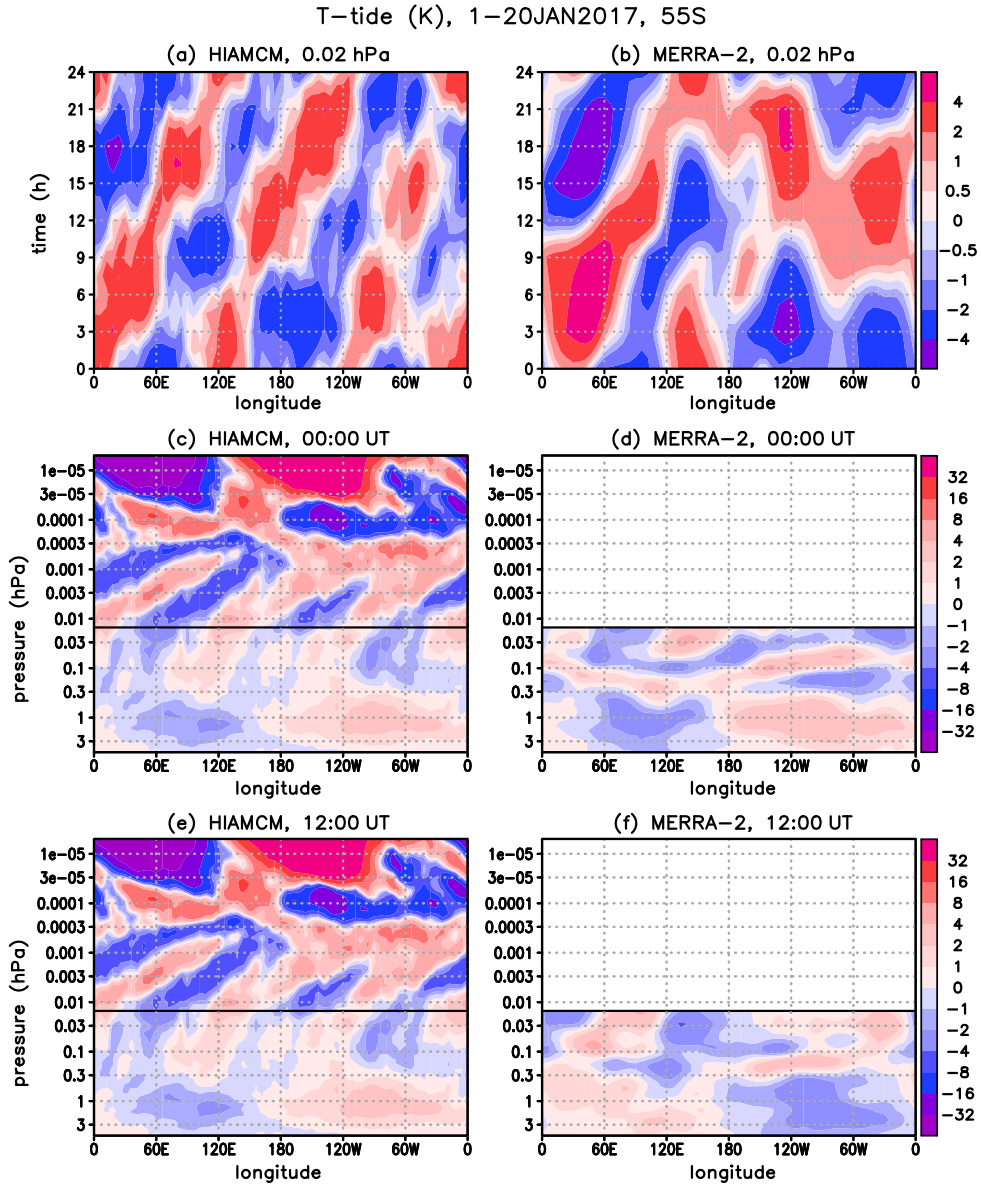


Figure 1. Temperature tide (K) at 55°S for 1-20 January 2017 from the HIAMCM (left column) and from MERRA-2 (right column). First row: Longitude-time plots at 0.02 hPa. Second (third) row: Longitude-height plots at 0 UT (12 UT).

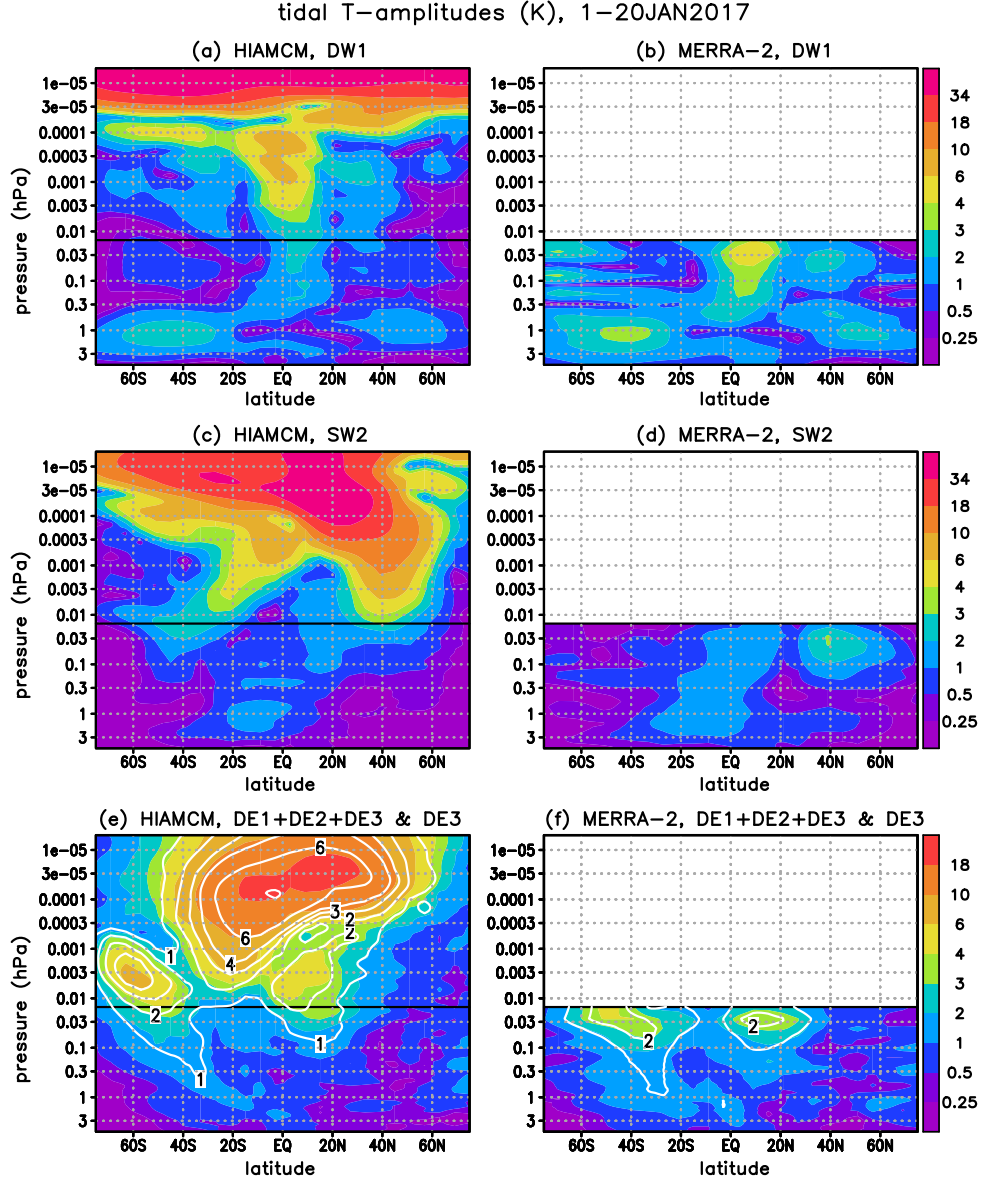


Figure 2. Tidal temperature amplitudes (K) for the 1-20 January 2017 period from the HIAMCM (left column) and from MERRA-2 (right column). First row: DW1. Second row: SW2. Third row: Sum of eastward propagating diurnal tides with zonal wavenumbers $s = 1$ to 3 (DE1+DE2+DE3, colours) and amplitude of the DE3 (white contours for 1, 2, 3, 4, 6, 8 K).

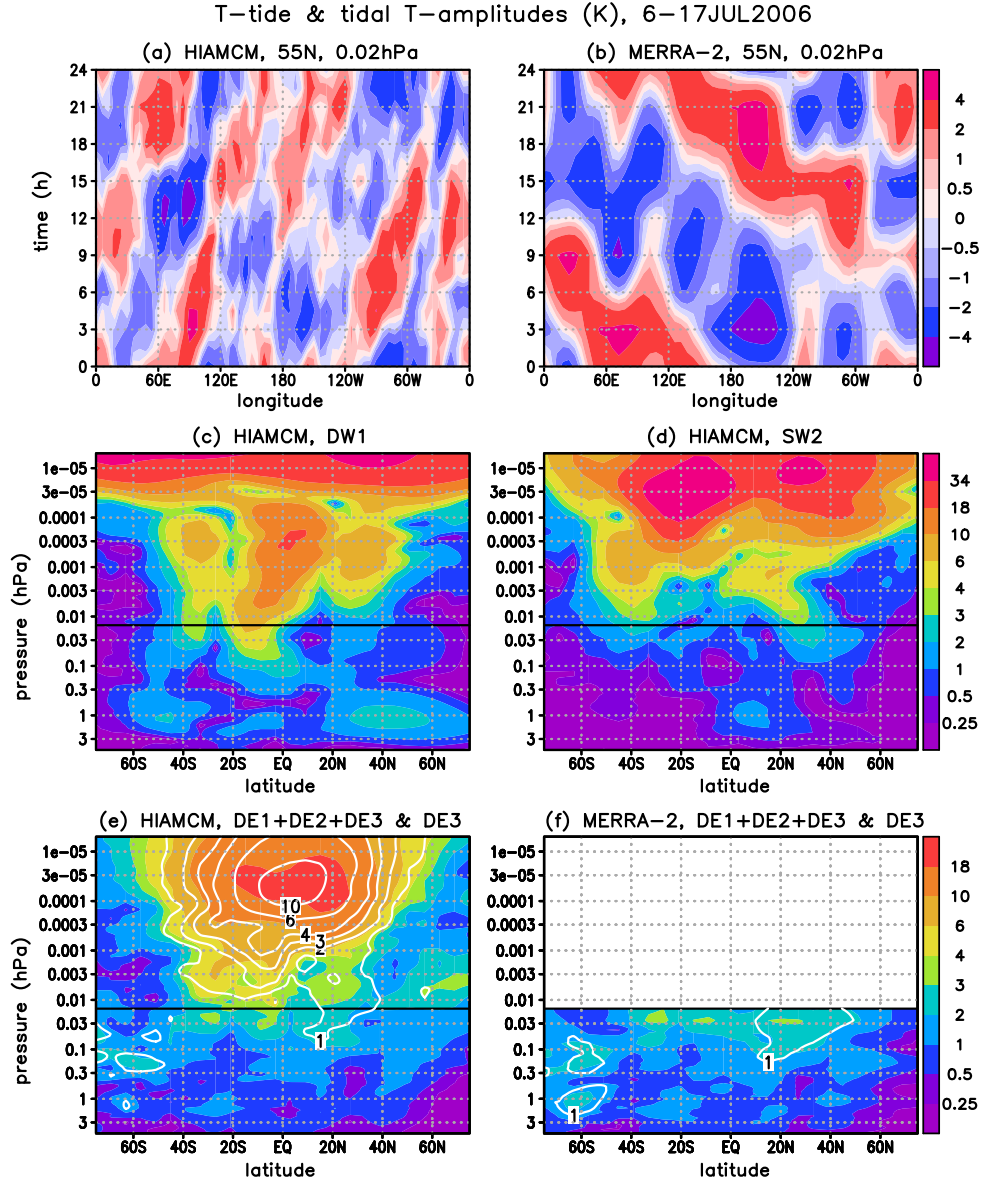


Figure 3. (a),(b) Same as Fig. 1a,b, but for 6-17 July 2006 and at 55°N. (c),(d) Same Fig. 2a,c, but for 6-17 July 2006. (e),(f) Same Fig. 2e,f, but for 6-17 July 2006.

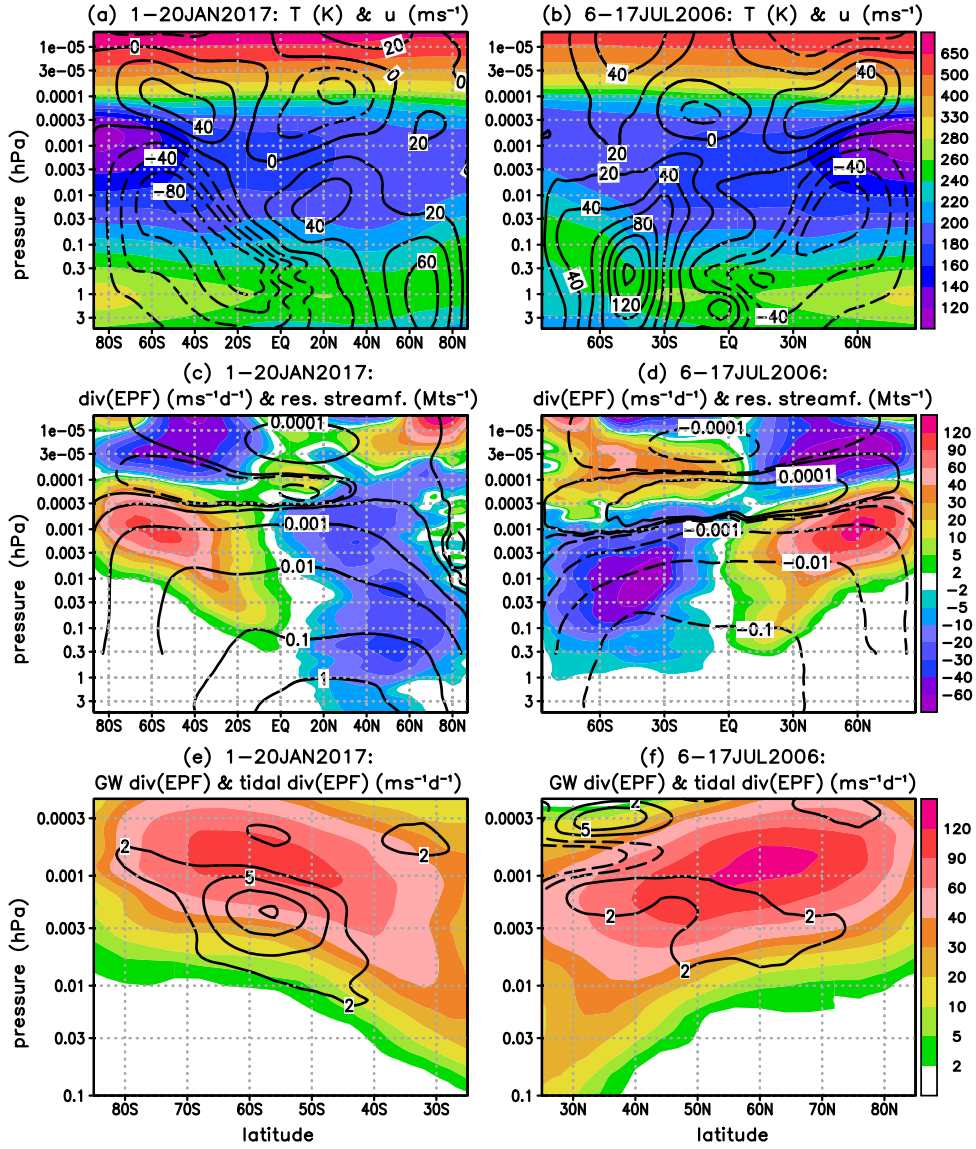


Figure 4. Zonal-mean circulation and wave driving from the HIAMCM for 1-20 January 2017 (left) and 6-17 July 2006 (right). First row: Temperature (colours) and zonal wind (contour interval 20 ms^{-1}). Second row: EPF divergence (colors, unit $\text{m s}^{-1}\text{d}^{-1}$) and residual mass streamfunction (contours for $\pm 10^{-4}, \pm 10^{-3}, +0.01, +0.1, +1 \text{ Mt s}^{-1}$ in (c) and for $\pm 10^{-4}, \pm 10^{-3}, -0.01, -0.1 \text{ Mt s}^{-1}$ in (d), $1 \text{ Mt} = 10^9 \text{ kg}$). Third row: EPF divergence due to GWs (colors, unit $\text{m s}^{-1}\text{d}^{-1}$) and tides (contours for $\pm 2, \pm 5, 10, 15 \text{ m s}^{-1}\text{d}^{-1}$) in the summer mesosphere.

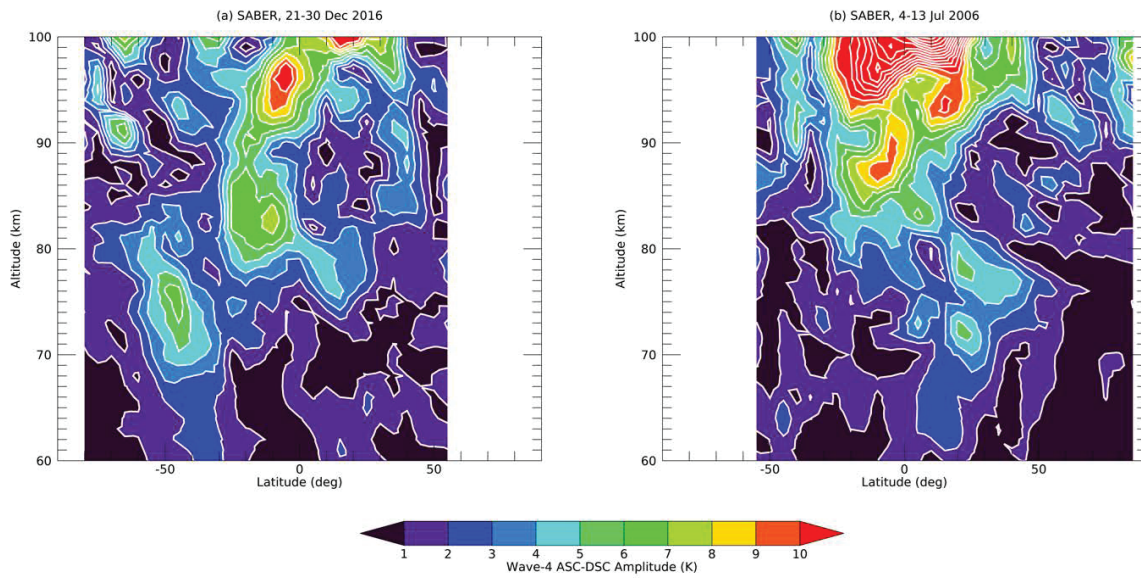


Figure 5. DEDE3 temperature amplitude estimates from SABER for (a) 21-30 December 2016 and (b) 3-13 July 2006: SABER wave-4 asc-dsc difference amplitudes. The amplitudes need to be divided by a factor of 2 for comparison with Figs. 2e,f and 3e,f.